MODELLING APPROACHES ON THE LUMBAR SPINE BIOMECHANICS - A COMPARATIVE STUDY

SOFIA P. FARIA*, PAULO R. FERNANDES* AND JOÃO O. FOLGADO*

* LAETA, IDMEC, Instituto Superior Técnico
Universidade de Lisboa
Av. Rovisco Pais, 1049-Lisboa, Portugal
e-mail: sofiafaria@tecnico.ulisboa.pt, prfernan@dem.ist.utl.pt, jfolgado@dem.ist.utl.pt

Key words: Finite Element Model, Lumbar Spine, Functional Spinal Unit, Density - Elasticity Relationship

1 INTRODUCTION

Spinal diseases are of major interest due to the high rate of morbidity and increasing healthcare costs. To avoid such an economical burden in individuals and government's expenditures, preventive measures and carefully chosen treatment modalities should be undertaken [1]. Among the several options available to study the biomechanics of the spine, Finite Element Models (FEM) emerge as a promising tool that allows for an accurate study of such intricate systems with material nonlinearities and heterogeneities as the biological tissues. Its capability of representing complex geometries and material properties divided into small discrete elements offers several advantages over the *in vivo* or *in vitro* experimental methods and other mathematical tools, particularly in stress and strain measurement and distribution.

Regarding the modelling process, a growing trend is to study patient-specific models rather than a generic anatomical representation of a vertebra or an intervertebral disc. For this purpose, two concepts must be considered: the geometric model and the material properties of the structures in question. For the first item, the geometry can be obtained through the multiple medical imaging modalities nowadays clinically available, such as CT or MRI. After acquisition, segmentation and superficial mesh techniques permit the formation of a solid model which can be utilised by a FE software. Although the majority of studies adopt this procedure for geometry, the dependence of material properties changes is often neglected. In spine modelling, authors frequently opt to simplify the bone constituents by assigning only two materials: a cortical shell with fixed thickness with a given Young's Modulus (E) and Poisson's Ratio (ν), and filling the interior with trabecular bone, which has a different Young's Modulus and Poisson's Ratio [2].

To circumvent this simplification and offer greater clinical value to the model, bone density information can be extracted from CT data. By virtue of CT numbers, measured in Hounsfield Units (HU), a direct relation can be established with density values. An HU measures the linear attenuation coefficient of the X-ray beam when it passes through water. The HU numbers for other material in the CT acquisition with a given linear attenuation coefficient μ_x are given by:

$$HU = \frac{\mu_x - \mu_{water}}{\mu_{water} - \mu_{air}} \times 1000 \quad (1)$$

where μ_{water} and μ_{air} are the linear attenuation coefficients for water and air, respectively. These two materials have a known density providing a calibration relation between densities and CT numbers to the CT machine. Afterwards, a material mapping of the FEM mesh can be done, hence the different properties can be found on each point of the model [3].

Currently, available commercial CT scanners are calibrated with the help of an external reference phantom, which contains reference materials similar to those present in body tissues. Phantoms are placed under the patient during scanning and equivalent densities are determined by comparison between the attained values in the patient's body and in the phantom [3].

Although the method accounts for scan-to-scan and scanner-to-scanner variability, the peripheral placement of the calibration system results in a measurable degradation in precision due to patient-moderated artifacts, partial volume averaging and repositioning errors [4,5,6].

Patient-moderated artifacts account for scatter and beam hardening. The former occurs because non-symmetrical objects appear in the X-ray path, resulting in different path lengths. The latter relates to the polychromatic nature of the beam in which for the same material, the edges appear brighter than the center. This occurs because the lower energy spectrum is more readily attenuated than the higher energies. The end result is a beam that, though diminished in overall intensity, has a higher average energy than the incident beam. Partial Volume Effects (PVE) occur due to tissue inhomogeneity, since one pixel might contain several substances/tissues, but since its value will be the average, blurring will inevitably exist and propagate to its neighboring pixels. Positioning errors also happen because manually chosen ROI's are weakly reproducible [4,5,6].

To improve reproducibility and accuracy of the results, over the last two decades, several authors have proposed a phantom-less method that uses the patient body tissues as the calibration reference. The proximity of the tissues to the vertebral bodies, for instance, avoid the reported errors and its easy implementation would have widespread clinical utility and cease quantitative information in any type of CT scanner that is currently available but not utilized [3,4,5,6,7.8].

Additional to CT-density calibration, the relationship between density and Young Modulus in bone remains controversial. Several empirical density-elasticity relationships to cortical and trabecular bone have already been established, but they have shown to be highly dependent on the experimental techniques implemented and its extrapolation to density values outside the samples density range have shown low correlation [9].

This work adapted a phantomless method based on fat and paraspinal muscle CT values to find bone density values and compared several density-elasticity relationships from Helgason et al. [9] review for both non-calibrated and calibrated scan acquisitions. This models were alongside compared with a homogeneous model, with values derived from literature. The effect of bone density variation in a L4-L5 functional spinal unit (FSU) was evaluated through stress distribution, intradiscal pressure (IDP) and range of motion (ROM).

2 METHODS

403 CT images of a 33 year-old woman were acquired by a Toshiba Aquillion scanner at 135 kVp, 350 mA and 1 mm slice thickness. Mimics® was used for image processing and segmentation, which combined with 3d-Matic, provided a pre-processing of the superficial meshes that allowed for triangle reduction and elimination of artifacts. A Point Cloud File was obtained and imported into Solidworks©, and with the help of Scanto3D Module, the superficial mesh was restored and smoothed. The mesh was converted into surfaces and finally into a solid model. A Parasolid file was imported into Abaqus®, where the FEM analysis could be attained. Density-based models had an additional step, where a specific mesh was chosen and again imported back to Mimics. Back there, density distribution and material properties were assigned through the mesh elements. The mesh was then returned to Abaqus and the analysis proceeded. A summary of the procedure is shown in Figure 1.

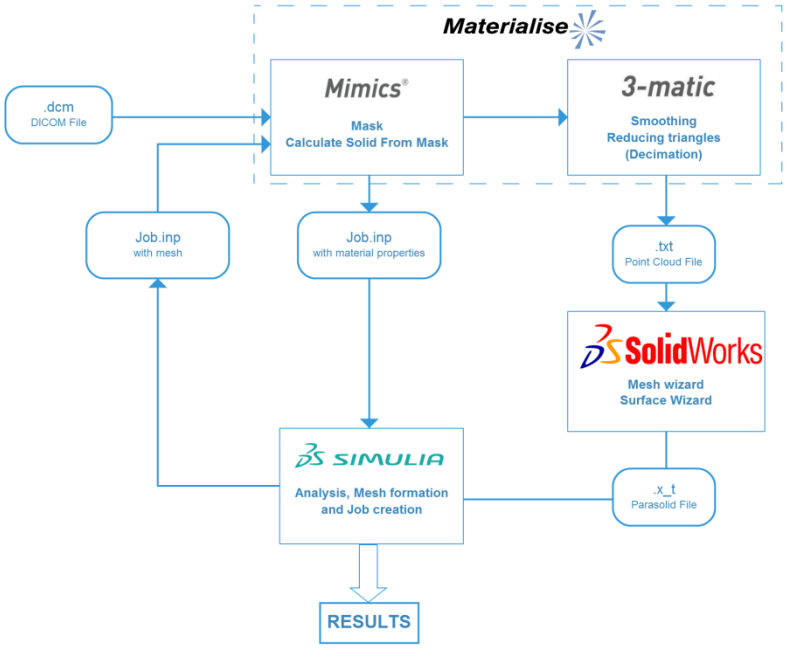

Figure 1: Methodology used for the developed model.

2.1 Non-calibrated bone density distribution

To verify how the system's calibration might influence the density values, a non-calibration condition was evaluated. For this case, one assumes that no non-linearities in the detector system occurs and that a linear relationship between CT values and material's density exists.

For the matter of notation, let CT correspond to the "measured HU values" and CTH correspond to the "corrected HU values". For a non-calibrated system, CT=CTH such that the HU-ρ relationships is:

$$\rho = a + bCT \tag{2}$$

where a and b are constants resulting from the regression law and ρ is given in gcm^{-3}. In HU scale, the linear relation must extend from CT number for air to a CT number for most

mineralized cortical bone. Selecting two regions of interest (ROI's) in Mimics containing the minimum CT value for air ($CT_{air} = -981$ HU) the maximum value for bone ($CT_{bone} = 1442$ HU) and knowing the densities for each material ($\rho_{air} = 0\ gcm^{-3}$ and $\rho_{bone} = 1.92\ gcm^{-3}$), the resulting relation was:

$$\rho = 0.777350392 + 7.924061081 \times 10^{-4}\ CT \quad (gcm^{-3}) \tag{3}$$

2.2 Calibrated bone density distribution

As previously described, Hounsfield scale is usually calibrated to water at 0 HU. Unfortunately, this substance may not be available during the scanning and its effective energy is not always known. By effective energy, one means "the single photon energy at which the linear attenuation coefficient of a particular material equals the linear attenuation coefficient in the polyenergetic beam". It depends on the material being scanned and on the position within the object [10].

As an alternative, fat and skeletal muscle have fixed compositions, with water in their constituents, and known linear attenuation coefficients as a function of X-ray effective energy, thus providing a way to plot a standard calibration curve [10].

Manipulating equation (1) to obtain the difference between HU values for muscle and fat, one obtained:

$$HU_{muscle} - HU_{fat} = \frac{\mu_{muscle} - \mu_{fat}}{\mu_{water}} \times 1000 \tag{4}$$

and considering the real value of $HU_{water} = CTH_{water} = 0$ one could find the following ratio:

$$-\frac{HU_{fat}}{HU_{muscle} - HU_{fat}} = \frac{\mu_{muscle} - \mu_{fat}}{\mu_{muscle} - \mu_{fat}} \tag{5}$$

to be a remarkable consistent value of 0.77 for measured CT values between 60 keV and 80 keV of effective energy, which correspond to tube peak voltages in the range of 120-140 kVp [7]. The measured HU values CT are then related to the corrected HU values CTH by

$$CTH = kCT + B \tag{6}$$

where k is the slope and B is the offset [7].

Two different ROI's containing only either fat or muscle were manually selected near the vertebral bone region. The pixel data was inserted in a Matlab routine to plot an histogram and obtain the most frequent CT value in each ROI, as depicted in Figure 2. The values found for fat and muscle were $CT_{fat} = -97$ and $CT_{muscle} = 53$, respectively.

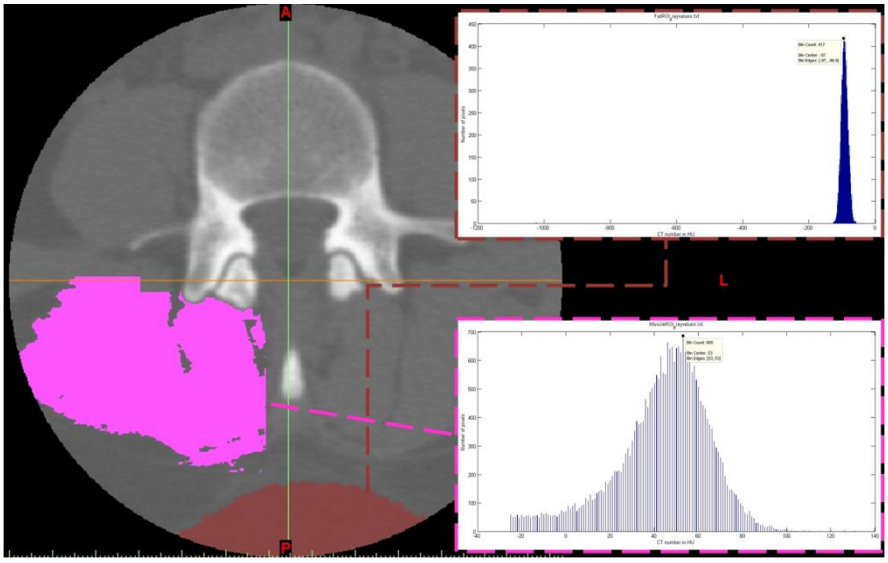

Figure 2: ROI selection for fat (red) and paraspinal muscle (pink) and respective histogramswith the most frequent CT value for each.

A tube voltage of 135 kVp corresponds, approximately, to its average in effective energy range of 70 keV and the corrected values were given by solving a two unknowns linear system (6) which resulted in

$$CTH = 1.0019CT - 17.361 \tag{7}$$

Values for CTH_{fat} and CTH_{muscle} are supplied by literature.

The adjustment (7) was inserted into equation (2) giving the new HU-ρ relation:

$$\rho = 0.791081265 + 7.909033917 \times 10^{-4}\, CT \quad (gcm^{-3}) \tag{8}$$

2.3 Young Modulus Mathematical Relationships

For the material properties, no global mathematical relationship exists between Young modulus (E) and density. Therefore, several experimental relations found on Helgason et al. article [9] were applied to the material distribution. These relations are found in Table 1.

Table 1: Density-elasticity mathematical relationships used from [9].

Study	E [MPa]	R^2
Morgan et al.(2003)	$E = 4730\rho_{app}^{1.56}$	0.73
Keller(1994)	$E = 1890\rho_{ash}^{1.92}$	0.702
Kopperdahl(1998)	$E = 2100\rho_{app} - 80$	0.61
Carter and Hayes(1977)	$E = 3790\dot{\varepsilon}^{0.06}\rho_{app}^{3}$	Not specified

Ash density= $\rho_{ash} = 0.60\rho_{app}$; Strain Rate= $\dot{\varepsilon} = 1$

A total of 25 different bone materials were assigned in Mimics for the heterogeneous models. Besides these heterogeneous models, a homogeneous model containing only trabecular bone and a cortical shell with 0.35 mm thickness was developed. The properties

and element type for each component of the L4-L5 segment are presented in Table 2.

Table 2: Material Properties and element types for the simplified model. AF, NP and CE are also applicable to heterogenous models.

	E [MPa]	Poisson's Ratio (ν)	Element type
Cortical Bone	12000	0.3	M3D3
Trabecular Bone	100	0.2	C3D4
Annulus Fibrosus (AF)	4.2	0.45	C3D4
Nucleus Pulposus (NP)	Incompressible fluid - filled cavity		SFM3D4
Cartilage Endplates (CE)	24	0.46	M3D4

Tie constraints were assigned between disc vertebrae interfaces and between Nucleus Pulposus (NP) and Annulus Fibrosus (AF) in the IVD. A fluid-cavity interaction was implemented in the NP to behave like a liquid with $\rho = 1.125\ gcm^{-3}$ and a frictionless surface-to-surface interaction was applied in the facet joints of the posterior elements.

Lastly, concentrated forces and moments were applied to the upper surface of L4 vertebra and a point on the lower surface of L5 was defined as encastre, with these conditions propagating to the neighbor elements as coupling constraints.

3 RESULTS

The comparison between the several models was made through stress distribution, IDP pressure and ROM and validated with data from Dreischarf et al. [11]. Differences in stress distribution were evaluated after applying a pure compressive load of 460 N. IDP was evaluated in Nucleus Pulposus pressure in three compressive load magnitudes of 300 N, 460 N and 600 N to preview its growing behaviour. ROM was tested in each axis direction, representing a movement within the physiological range. Adding to ROM, a pre-load is imposed with a compressive force to mimic disc's compression in real scenarios.

3.1 Stress distribution

Stress distribution varied from homogeneous to the heterogeneous models, whereas differences between the calibrated heterogeneous and non-calibrated heterogeneous models were less evident.

In the homogeneous model, stresses tended to concentrate in the outer cortical shell, mostly in the vertebral body rather than in posterior elements. Being a compressive force, they were anteriorly distributed, with higher magnitude in L5 vertebra and also in the anterior part of the AF. Note that, as the material limits were well defined, so did the rapid change in stress distribution from the cortical to the trabecular bone.

In the heterogeneous models, for the several density-elasticity relationships, the stress patterns were very similar, showing a bigger spread of the stress from the outer surface to the inner material. However, the higher stresses appeared to form a shell boundary near the surface, suggesting regions of higher density similar to the one simplified in the homogeneous model. The stresses in vertebrae were one order of magnitude lower than in the first model,

but the stresses in the AF were of the same order. Between calibrated and non-calibrated models, the variation in stress occurred only in the third decimal order for all $\rho - E$ relations except for Kopperdahl. The differences for Kopperdahl relation are shown in Figure 3.

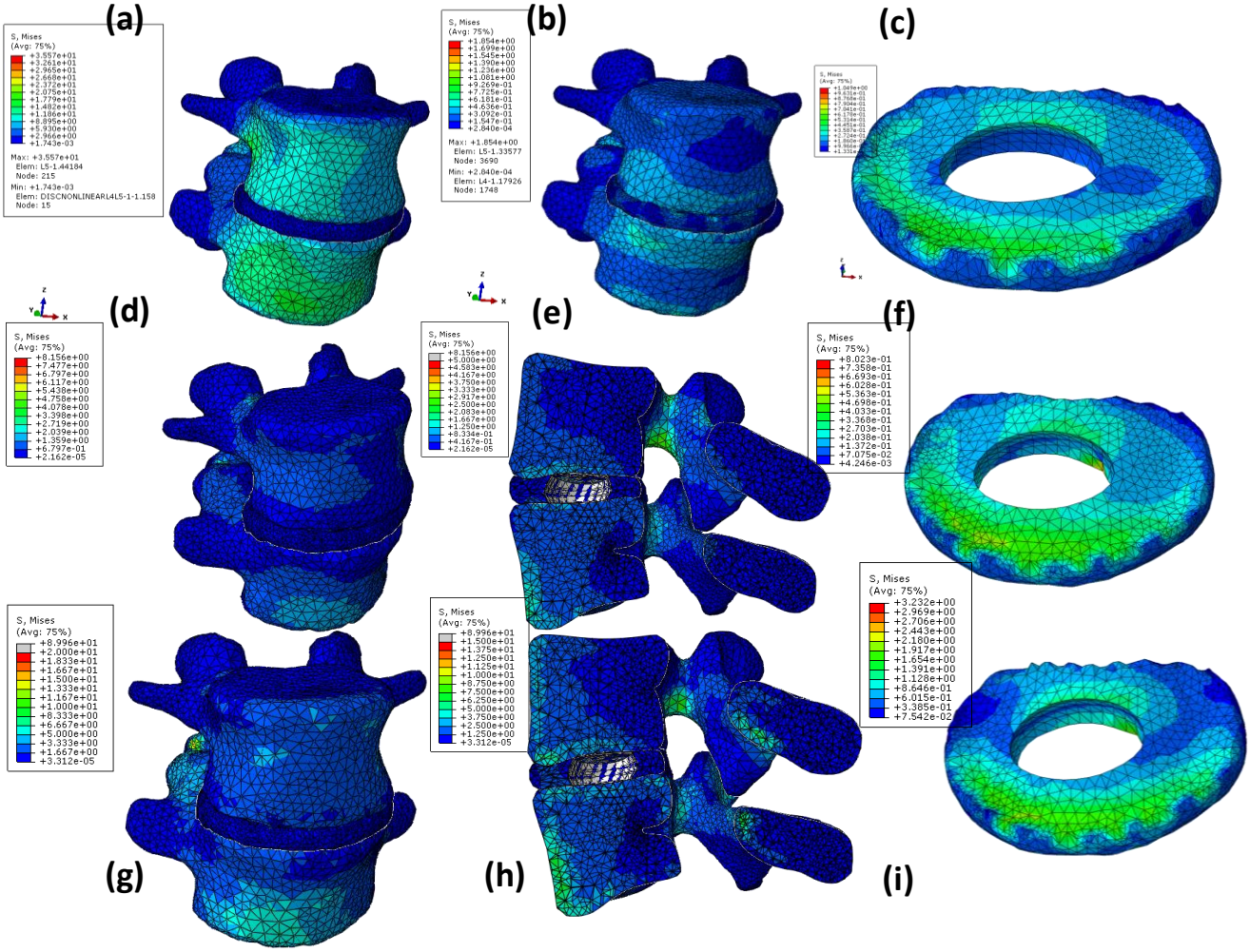

Figure 3: Von Mises stress distribution when applying a compressive force of 460N in (a) cortical shell (b) trabecular bone of the homogeneous model, (c) AF of the homogeneous model, (d) and (e) calibrated Kopperdahl model, (e) and (h) non-calibrated Kopperdahl model, (f) calibrated and (i) non-calibrated Kopperdahl AF model.

3.2 Intradiscal pressure

IDP values for the homogeneous and heterogeneous linear models showed a growing linear trend when applying greater loads. Comparing to the Dreischarf et al. [11], in Figure 4, both homogeneous and heterogeneous models showed greater IDP than the *in vivo* values, but were within the limits of the computational models reviewed in the article, which avoided their invalidation.

Homogeneous model showed lower IDP values than heterogeneous models, and between the calibrated and non calibrated equations, IDP values appeared to be the same. In terms of density-elasticity relations, the Keller model had closer values to the homogeneous model and

also the *in vivo* values of the article. IDP for all models are organized in Table 3.

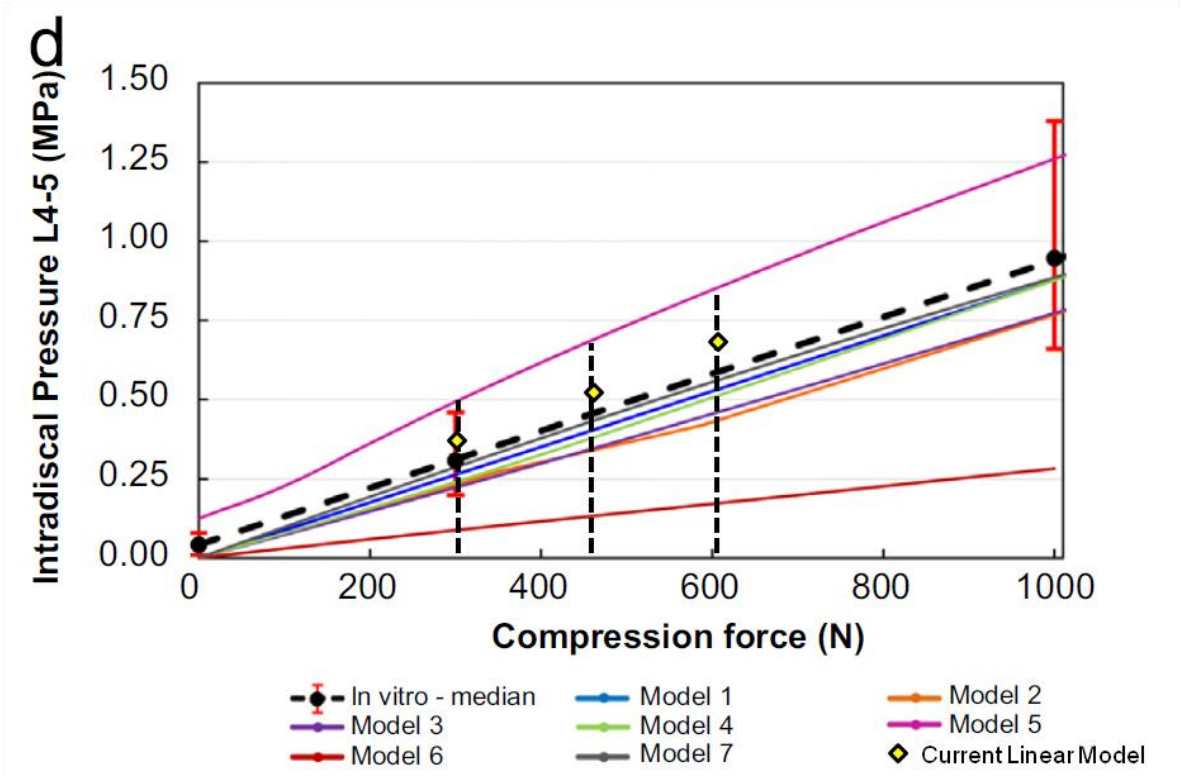

Figure 4: Image adapted from Dreischarf et al. [11] containing the IDP values for *in vivo*(dark dashed line) and computational models (model 1-7) in comparison with the obtained values for the homogeneous model (yellow dots).

Table 3: Intradiscal pressure for the homogeneous model and for the calibrated and non-calibrated models with different density-elasticity relationships. All values are in MPa.

Compressive Force	Homogeneous Model (MPa)	Carter and Hayes (MPa)		Keller (MPa)		Kopperdahl (MPa)		Morgan (MPa)	
		NC	C	NC	C	NC	C	NC	C
300 N	0.336	0.375	0.375	0.369	0.368	0.372	0.372	0.375	0.375
460 N	0.515	0.575	0.575	0.564	0.564	0.571	0.571	0.575	0.575
600 N	0.670	0.760	0.760	0.736	0.736	0.745	0.745	0.760	0.760

3.3 Range of motion

Except for flexion, all movements in the three models show similar values to the ones exhibited *in vivo* and were within the range of ROM values predicted from computational models considered in Dreischarf et al. [11], as depicted in Figure 5.

Nevertheless, one noticed that homogeneous model overestimated ROM values and even exceed the physiological range for axial rotation, whereas the heterogeneous models did not display such exaggerated behavior. Juxtaposing the calibrated and non-calibrated models, the values were always very similar, although some differences existed in flexion/extension and

in lateral bending movements.

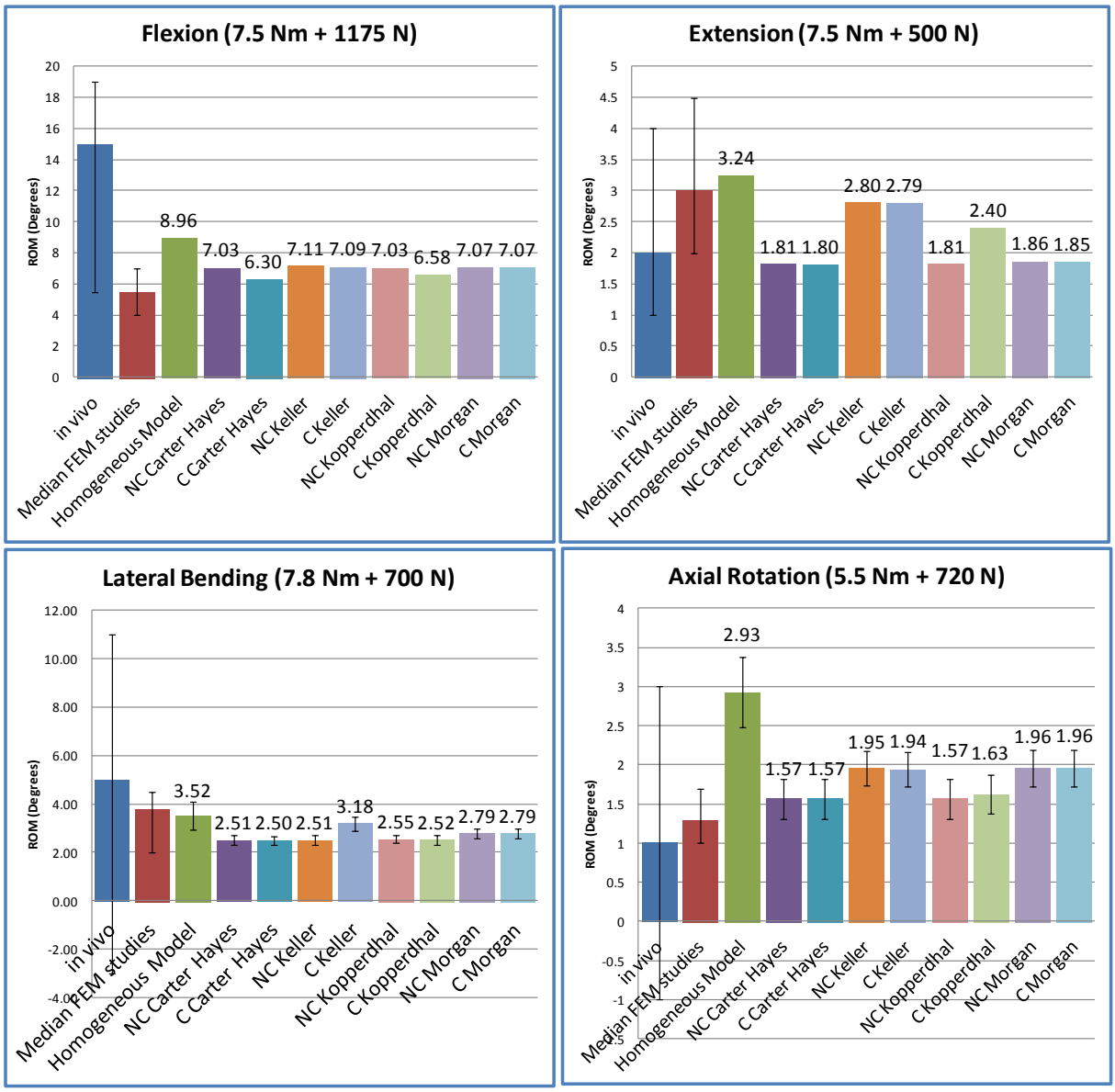

Figure 5: Range of Motion in *(a)*flexion, *(b)*extension, *(c)* lateral bending and *(d)*axial rotation for the homogeneous model (darker green), the different non-calibrated (NC) and calibrated heterogeneous models (C), in comparison with Dreischarf et al. article [11] for *in vivo* (dark blue) and FEM models (dark red). For *(c)*lateral bending and (*d)*axial rotation the average value for left and right movements is given and bars represent maximum and minimum deviation. Median FEM bar represents the average value for a total of six studies presented in [], with maximum and minimum values. *In vivo* bar represents the average value for each movement from a population of individuals, with maximum and minimum values.

4 DISCUSSION

The results for an L4-L5 FSU were within the expected ranges and showed similarity to literature. The work evaluated the influence of heterogeneity of vertebral density and also the

influence of CT calibration in the biomechanical behaviour of the segment through stress distribution, IDP and ROM.

Stress distribution when applying a compressive force showed the similar patterns for density-elasticity relationships, making anterior L5 cortical shell to bear the higher stresses. Differences within the stress values were noted although they were always in the same range and order of magnitude. For differences between calibrated and non-calibrated models, the same happened with exception for Kopperdahl model. This was the only linear density-elasticity relationship and since calibration equation corrected the CT numbers in terms of offset and linear slope, this was directly observed in a linear density-elasticity relationship. The effect is seen in the proximity of trabecular bone stress distribution that in the calibrated model approaches the homogeneous one, whereas the non-calibrated model showed higher values.

The stress distribution in AF also agreed with the noticed differences for calibrated Kopperdahl and non-calibrated Kopperdahl models. While homogeneous and calibrated models were in the same order of magnitude, non-calibrated presented higher values for stress. All models presented higher stresses in the anterior part of AF, as expected in response to a compressive force, but in the homogeneous model the higher stresses were more concentrated in anterior part than for both heterogeneous models. This effect was expected since the cortical shell had a well defined limit of 0.35 mm, where the bone is stiffer.

Intradiscal pressure was measured applying compressive forces of 300N, 460N and 600N in Nucleus Pulposus, where an incompressible fluid was simulated. All heterogeneous models showed higher IDP than the homogeneous model and between calibrated and non-calibrated models IDP values were identical. The fact that homogenous model presented a cortical shell that concentrated higher stresses in the anterior outer surface of the vertebral bodies when a compressive force was applied, alleviated the stress distribution in the inner part of AF, hence a bigger deformation of NP was allowed and IDP was reduced in comparison to heterogeneous models.

In comparison to values in literature, IDP was higher than *in vivo* and some computational models but remained within the predicted range. One reason might relate to the influence of disc's height, since the present model had a smaller value than the reported ones in Dreischarf et al. [11].

ROM value were evaluated when simulating physiological loading conditions. A pre-load was applied to assure disc pressurization, as happening *in vivo* due to upper body's weight. Except for flexion, all values were similar to the ones presented in literature, but in axial rotation they seem to be slightly higher than *in vivo* average.

Between homogeneous and heterogeneous models, the latter presented smaller ROM in all movements due to the higher stiffness of vertebrae. Among calibrated and non-calibrated models, some differences were noted when the disc suffered higher compression. In flexion/extension, the smaller differences observed showed higher movement for non-calibrated models, were the bone density offered a wider range between cortical and trabecular bone, than the calibrated models. In lateral bending the difference is observed exclusively in calibrated Keller model, possibly due to a proximity of bone density distribution to the homogeneous model.

Axial rotation was above the reported values in all models because it greatly depends on the disc modelling. The present IVD was chosen to be a linear isotropic material, whereas all

discs presented in literature were modelled as nonlinear materials, containing radially distributed collagen fibres layers embedded in a non-elastic ground substance material. Collagen layers have an important role when under tension, dictating preferential fibre directions, which have a critical effect in axial rotation [12]. Since linear elasticity does not account for this effect, the present models showed higher values in axial rotation movements than the ones in Dreischarf et al. [11].

Besides IVD modelling, some limitations in this work should be mentioned. In the CT-ρ relationships, a total of 25 types of materials for bone were considered. A higher number could have been chosen to increase the resolution in order to see the cortical layer more clearly. Differences between calibrated and non-calibrated equations were not so evident as expected, so other patient and/or other scan should be as well evaluated to verify if the results changed or not. Several density-elasticity relationships have been reported for vertebral bone but the wide range of values they offer and low correlation values do not allow the investigator to opt for only one.

When establishing these CT-ρ and ρ-E relationships, their influence in stress analysis and distribution should be taken into consideration, and their use in clinical practice, for example, for osteoporosis or spinal implant fixation planning, must be carefully made, because they are susceptible to high variability.

5 CONCLUSION

- Heterogeneity in bone distribution of vertebrae showed influence in stress distribution, intradiscal pressure and range of motion values. Higher values in intervertebral disc stress and intradiscal pressure were noted when heterogeneous models were applied rather than the commonly used homogeneous models of literature. Range of motion was smaller in heterogeneous models than in the homogeneous models but more similar to the ones verified *in vivo*.
- Effect of calibration in density values had less impact although further study with other scan settings and/or individuals should be made, as well as studying other loading conditions.

6 ACKNOWLEDGMENTS

The authors would like to thank Quadrantes Clinic in Miraflores for providing the CT images.

REFERENCES

[1] Hoy, D., March, L., Brooks, P., Blyth, F., Woolf, A., Bain, C., ... & Buchbinder, R. The global burden of low back pain: estimates from the Global Burden of Disease 2010 study. *Annals of the rheumatic diseases* (2014), **73**(6): 968-974.

[2] Kurutz, M. *Finite element modelling of human lumbar spine*. INTECH Open Access Publisher, (2010).

[3] Celenk, C., & Celenk, P. *Bone density measurement using computed tomography*. INTECH Open Access Publisher, (2012).

[4] Mueller, D. K., Kutscherenko, A., Bartel, H., Vlassenbroek, A., Ourednicek, P., & Erckenbrecht, J. Phantom-less QCT BMD system as screening tool for osteoporosis

without additional radiation. *European journal of radiology* (2011), **79**(3): 375-381.

[5] Kopperdahl, D. L., Lee, D. C., & Keaveny, T. M. *U.S. Patent No. 20,140,376,701*(2014). Washington, DC: U.S. Patent and Trademark Office.

[6] Boden, S. D., Goodenough, D. J., Stockham, C. D., Jacobs, E., Dina, T., & Allman, R. M. Precise measurement of vertebral bone density using computed tomography without the use of an external reference phantom. *Journal of digital imaging* (1989), **2**(1), 31-38.

[7] Gudmundsdottir, H., Jonsdottir, B., Kristinsson, S. E., Johannesson, A., Goodenough, D., & Sigurdsson, G. Vertebral bone density in Icelandic women using quantitative computed tomography without an external reference phantom. *Osteoporosis International* (1993), **3**(2), 84-89.

[8] Zhao, K., Pan, X. G., Zou, Y. Y., Wang, Z. Q., Zhang, T. J., Shao, K., ... & Zhao, H. An automatic method for measurement of vertebral bone density based on QCT without an external reference phantom. In *Sixth International Symposium on Multispectral Image Processing and Pattern Recognition* (pp. 74972I-74972I). International Society for Optics and Photonics (2009).

[9] Helgason, B., Perilli, E., Schileo, E., Taddei, F., Brynjólfsson, S., & Viceconti, M. Mathematical relationships between bone density and mechanical properties: a literature review. *Clinical Biomechanics* (2008), **23**(2), 135-146.

[10] Tofts, P. S., & Sank, V. J. (1981). Definitions of effective energy in computed tomography. *Journal of Computer Assisted Tomography*, *5*(6), 950.

[11] Dreischarf, M., Zander, T., Shirazi-Adl, A., Puttlitz, C. M., Adam, C. J., Chen, C. S., ... & Schmidt, H. Comparison of eight published static finite element models of the intact lumbar spine: predictive power of models improves when combined together. *Journal of biomechanics* (2014), **47**(8), 1757-1766.

[12] Schmidt, H., Galbusera, F., Rohlmann, A., & Shirazi-Adl, A. What have we learned from finite element model studies of lumbar intervertebral discs in the past four decades?. *Journal of biomechanics*(2013), **46**(14), 2342-2355.